frontiers in Materials

ORIGINAL RESEARCH
published: 14 August 2020
doi: 10.3389/fmats.2020.00278

Microstructure and Mechanical Properties of AZ31/ZrO_2 Composites Prepared by Friction Stir Processing With High Rotation Speed

Qianhao Zang[1], Xiaowen Li[2], Hongmei Chen[1], Jing Zhang[3], Ling Wang[4], Shujin Chen[1], Yunxue Jin[1] and Sheng Lu[1]*

[1] School of Materials Science and Engineering, Jiangsu University of Science and Technology, Zhenjiang, China, [2] Shandong Heavy Machinery Co., Ltd., Linyi, China, [3] School of Metallurgy and Materials Engineering, Jiangsu University of Science and Technology, Zhenjiang, China, [4] School of Materials Science and Engineering, Yingkou Institute of Technology, Yingkou, China

The nano-ZrO_2-reinforced AZ31 alloy composites were fabricated by friction stir processing with three multi-passes and high rotation speeds. The AZ31/2.14 vol% ZrO_2, AZ31/4.29 vol% ZrO_2, and AZ31/6.43 vol% ZrO_2 composites were designed. The fine microstructure and uniform dispersion of ZrO_2 particles were observed in the AZ31/ZrO_2 composites. The excellent interfacial bonding was observed between the Mg matrix and ZrO_2. The hardness and tensile properties were enhanced after three cumulative friction stir processing passes. This was attributed to grain refinement and strengthening effects of ZrO_2. The tensile properties and hardness of the AZ31/ZrO_2 composite increased with the increase of volume fraction of the ZrO_2 particles from 2.14 to 6.43 vol%.

Keywords: AZ31 alloy, Nano-ZrO_2 particles, friction stir processing, microstructure, mechanical properties

OPEN ACCESS

Edited by:
Lai-Chang Zhang,
Edith Cowan University, Australia

Reviewed by:
Hongwei Cui,
Shandong University of Technology, China
Hui Yu,
Hebei University of Technology, China
Lili Chang,
Shandong University, China

****Correspondence:***
Hongmei Chen
hmchen@just.edu.cn

Specialty section:
This article was submitted to Structural Materials, a section of the journal Frontiers in Materials

Received: *25 June 2020*
Accepted: *24 July 2020*
Published: *14 August 2020*

Citation:
Zang Q, Li X, Chen H, Zhang J, Wang L, Chen S, Jin Y and Lu S (2020) Microstructure and Mechanical Properties of AZ31/ZrO_2 Composites Prepared by Friction Stir Processing With High Rotation Speed. Front. Mater. 7:278. doi: 10.3389/fmats.2020.00278

INTRODUCTION

Mg alloys have some advantages, such as low density, high specific strength, and high damping capacity, which have been applied in automotive and aerospace industries (Suh et al., 2016; Zang et al., 2017; Zhang J. et al., 2017; Zhang L. C. et al., 2020). The Mg alloys and Mg-based composites with excellent mechanical properties have been developed to meet the large demand for light materials in automotive and aerospace industries (Zhang M. et al., 2017; Yu et al., 2018; Shahin et al., 2020). Recently, many studies were focused on the Mg-based composites by reinforcing Al_2O_3, ZrO_2, *SiC*, graphene, graphene oxide, etc. fabricated by *in situ* synthesis process, semi-powder metallurgy, and friction stir processing (FSP) (Li et al., 2017; Meng et al., 2018; Zhang et al., 2018).

Among these techniques for fabrication of Mg-based composites, FSP has attracted extensive attention, which could fabricate Mg-based composites efficiently due to frictional heating and severe plastic deformation (Del Valle et al., 2015; Liang et al., 2017). At the same time, FSP could refine the grain size, homogenize the microstructure, and improve the dispersion of reinforcements (Chen et al., 2015; Arab and Marashi, 2019; Zhang and Chen, 2019). Navazani and Dehghani (2016) investigated the microstructure and mechanical properties of AZ31/ZrO_2 composites fabricated by FSP. The refinement of the microstructure and fine dispersion of ZrO_2 particles were obtained after FSP, and the mechanical properties were improved. In the case of FSPed Mg-based composites, the tool geometry and the process parameter optimization (like capping pass, multiple passes) were extensively investigated to improve the mechanical properties (Hashemi and Hussain, 2015; Khodabakhshi et al., 2017; Barati et al., 2019). The distribution of reinforcement and the interfacial bonding between matrix and reinforcement largely determines its mechanical properties

(Sharma A. et al., 2019; Ajay Kumar et al., 2020). The previous researches have focused on FSPed Mg-based composites with the conventional rotation speeds (less than 2,000 rpm) (Hanas et al., 2018; Shang et al., 2019). High rotation speed FSP has advantages of fast heating rate, fewer process defects, a more stable process, good mechanical properties, and so on. The processing efficiency is high due to the high heat input during high rotation speed FSP (Chen et al., 2017). Liu et al. (2020) investigated the microstructure and mechanical properties of FSPed AZ31 alloy with high rotation speed, which shows excellent corrosion resistance and mechanical properties. The dispersion of β-$Al_{12}Mg_{17}$ precipitates increased with increased processing speed. Thus, the FSP with high rotation speed could improve the dispersion of particles. It is meaningful to investigate the microstructure and mechanical properties of Mg-based composites by FSP with high rotation speed.

In this work, AZ31-matrix composites reinforced with a different volume fraction of ZrO_2 particles were fabricated by the FSP process with high rotation speed. The microstructure and mechanical properties of FSPed AZ31/ZrO_2 composites fabricated by different FSP passes and volume fraction of ZrO_2 particles were investigated. The effects of FSP process and ZrO_2 particles on mechanical properties were discussed.

MATERIALS AND METHODS

Commercial AZ31 alloy plates with the desired size of 150 × 80 mm and a thickness of 2 mm were used as the matrix. The chemical composition of AZ31 alloy sheets is shown in **Table 1**. Commercial nano-ZrO_2 with an average diameter of 50 nm, purity >99.99 wt%, were used as reinforcing particles, purchased from Shanghai Macklin Biochemical Co., Ltd.

The grooves with three different dimensions of 1.5 mm (depth) × 0.2 mm (width), 1.5 mm (depth) × 0.4 mm (width), and 1.5 mm (depth) × 0.6 mm (width) were machined in the middle of the AZ31 alloy plates. Then, the grooves filled the ZrO_2 particles. The volume fraction of the ZrO_2 particles were approximately 2.14, 4.29, and 6.43%. This was calculated based on the method in Balakrishnan et al. (2015). At first, a capping pass with a cylindrical pin-less tool with a shoulder diameter of 7 mm was carried out, which can encapsulate the ZrO_2 particles and prevent them from ejecting during FSP process. This capping pass was applied to improve the stability in the preplaced ZrO_2 particles in the groove, which involves closing the top surface of the groove. Then, FSP was performed with a tool with a shoulder diameter of 7 mm and a pin length of 1.9 mm at a high tool rotation rate of 9,000 rpm, a travel speed of 200 mm/min, and a tilt angle of 3°. FSP with a different volume fraction of the ZrO_2 particles was carried out in one pass, two passes, and three passes, which is shown in **Table 2**. The temperature in the stir zone (SZ) was 383.8 ± 2°C during FSP, which was corrected by a k-type thermocouple.

TABLE 1 | Chemical composition of the AZ31 alloy (wt. %).

Al	Zn	Cu	Si	Mn	Fe	Al
2.52	0.91	2.00	0.02	0.22	0.01	Bal.

An optical microscope (OM) observation was performed on the cross-section of the FSPed samples. OM was observed after etched by 4.2 g picric acid, 10 ml acetic acid, 70 ml ethanol, and 10 ml H_2O for 10 s. Measuring of average grain size was carried out on OM images using Proimage software. The microstructure observation of ZrO_2 distribution in AZ31 matrix was performed by scanning electron microscopy (SEM, JSM-6610LV) and energy dispersive spectroscopy (EDS) at an accelerated voltage of 20 kV. The microstructure of ZrO_2 distribution in the AZ31 matrix was also observed by using JEM-2100F transmission electron microscope (TEM) at 200 kV. TEM specimens were collected from SZ and were twin-jet polished in a solution of nitric acid (10%), glycerin (30%), and methanol (60%) and, finally, ion-milled for 30 min. The phases of the AZ31 matrix and the composites were identified by an X-ray diffraction (XRD) analyzer (Bruker, D8 Advance) with a Cu target at a scanning angle of 20°–90° and a scanning speed of 4°/min. Microhardness mapping was performed across the thickness section of these FSPed samples. Vickers microhardness was measured on the FSPed samples, which was done at 0.1 kg load and dwell time of 10 s. The measurements were carried out on a grid of five parallel lines for the composites. A total number of 145 points (5 × 29) were used with an indent spacing of 0.5 mm. Microhardness mapping was performed using Matlab software. Tensile specimens were electrical discharge machined from the SZ parallel to the FSP direction, and the dimensions of tensile specimens are shown in **Figure 1**. The tensile test was conducted

TABLE 2 | Traverse speed and volume fraction of ZrO_2 particles for AZ31/ZrO_2 composites.

Specimen	Traverse speed (mm/min)	Volume fraction (%)	FSP pass
Z1-3P	200	2.14	3 passes
Z2-3P	200	4.29	3 passes
Z3-1P	200	6.43	1 pass
Z3-2P	200	6.43	2 passes
Z3-3P	200	6.43	3 passes

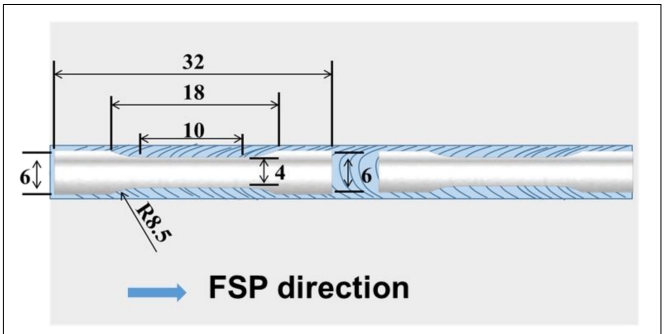

FIGURE 1 | Schematic illustration of the tensile test specimens.

at ambient temperature, and the velocity of the crosshead was 1.25 mm/min.

RESULTS AND DISCUSSION

Distribution of ZrO_2 Particles in FSPed AZ31/ZrO_2 Composites

Figure 2 shows the SEM-EDS mapping of the SZ-center in the AZ31/ZrO_2 composite (Z3-1P specimen) after one FSP pass; five major elements O, Mg, Al, Zn, and Zr are present. The white phases with O and Zr elements were observed in the FSPed AZ31/ZrO_2 composite. It indicated that ZrO_2 clusters existed in the FSPed AZ31/ZrO_2 composite after one FSP pass. The SEM-EDS mapping of the SZ-center in the AZ31/ZrO_2 composite (Z3-2P specimen) after two cumulative FSP passes is shown in **Figure 3**; segregation of Zr and O was still observed. The ZrO_2 clusters were obviously observed after one FSP pass, and the segregation significantly reduced when two cumulative FSP passes were applied.

Figure 4 shows the EDS elemental mapping analysis results from the microstructure of the FSPed AZ31/ZrO_2 composites (Z3-3P specimen) after three cumulative FSP passes. The EDS result (Point A: 50.37 at.% O, 36.19 at.% Mg, 3.24 at.% Al, 0.73, at.% Zn and 9.47 at.% Zr) suggested that the white particles were ZrO_2 particles. The SEM-EDS mapping also shows well-distributed ZrO_2 particles after three cumulative FSP passes, and it was observed to be free from clustering noticeably.

The agglomeration of ZrO_2 particles was easy to obtain due to insufficient plastic material flow with low heat input during a single FSP pass. The continuous clusters of ZrO_2 particles existed in the SZ of the Z3-1P specimen. The ZrO_2 particles did not distribute well in the matrix, and the agglomeration was unavoidable. The agglomeration of ZrO_2 particles reduced with increasing the FSP passes. The distribution of ZrO_2 particles was more uniform, with continuing the severe deformation up to three FSP passes. Vahedi et al. (2020) investigated the microstructure of FSPed AZ31 composites reinforced by micro-graphite and nano-graphene particles, and a similar

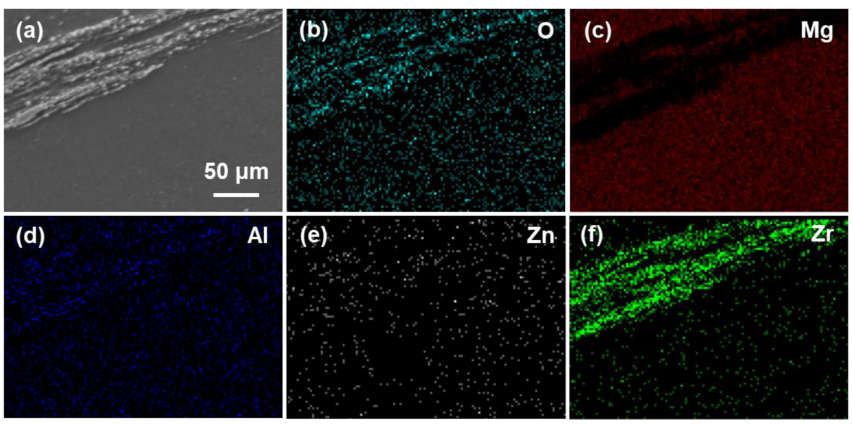

FIGURE 2 | SEM-EDS mapping shows **(a)** the ZrO_2 particles embedded in matrix **(b–f)** color mapping of elements O, Mg, Al, Zn, and Zr of the SZ-center in FSPed AZ31/ZrO_2 composite (Z3-1P specimen).

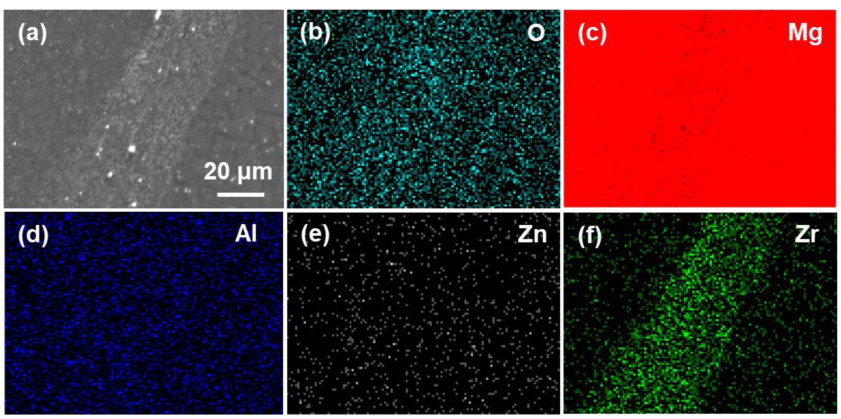

FIGURE 3 | SEM-EDS mapping shows **(a)** the ZrO_2 particles embedded in matrix **(b–f)** color mapping of elements O, Mg, Al, Zn, and Zr of the SZ-center in FSPed AZ31/ZrO_2 composite (Z3-2P specimen).

phenomenon was also observed. The well-distributed particles were obtained after the three FSP passes.

The distributions of ZrO_2 particles in the FSPed Z1-3P, Z2-3P, and Z3-3P specimens are shown in **Figure 5**. The SEM micrographs from SZ confirmed that there were no large agglomerations of ZrO_2 particles after three cumulative FSP passes with a different volume fraction of the ZrO_2 particles. The fraction of ZrO_2 particles in the SZ of the FSPed AZ31/ZrO_2 composites increased with the increase of the ZrO_2 addition, and more ZrO_2 particles were observed in the FSPed Z3-3P specimen. The better distributions of particles were observed in the FSPed Z1-3P, Z2-3P, and Z3-3P specimens.

Figure 6 shows the XRD patterns of AZ31 alloy and FSPed AZ31/ZrO_2 composites, and the Mg, β-$Al_{12}Mg_{17}$ phase were observed in AZ31 alloy. The Mg, β-$Al_{12}Mg_{17}$ phase and ZrO_2 phase diffraction peaks were observed in the FSPed Z1-3P, Z2-3P, and Z3-3P specimens. β-$Al_{12}Mg_{17}$ intermetallic is the most common and abundant in Mg-Al-Zn alloys. The results of XRD confirm the existence of ZrO_2 particles in the FSPed Z1-3P, Z2-3P, and Z3-3P specimens. Besides, it also suggested that no reaction occurred between the AZ31 alloy and ZrO_2 particles during the FSP. A similar phenomenon was also reported in Mazaheri et al. (2020), and the ZrO_2 particles were stable during the FSP.

Microstructure of Base Metal and FSPed AZ31/ZrO_2 Composites

Figure 7a shows the OM of the base metal AZ31 alloy plates, and the initial microstructure of the base metal was fine equiaxed grains and some coarse grains. Several fine equiaxed grains were observed in the SZ-center in the FSPed AZ31/ZrO_2 composite (Z3-3P specimen); see **Figure 7b**. The grain size of the SZ-center of the FSPed Z3 specimen was refined due to the occurrence of dynamic recrystallization during the FSP. A distinct boundary existed between the SZ and thermo-mechanically affected zone (see **Figure 7c**). The grain size increased in the thermo-mechanically affected zone, and some coarse grains were observed (see **Figure 7d**). **Figure 8** shows the OM of SZ-center of the FSPed AZ31/ZrO_2 composites (Z1-3P and Z2-3P specimens). The fine equiaxed grains were obtained in the SZ-center in the FSPed Z1-3P and Z2-3P specimens. The average grain sizes of SZ-center in the FSPed Z1-3P, Z2-3P, and Z3-3P were 8.46, 8.23, and 8.39 μm, respectively. A similar grain size was obtained in the SZ of FSPed AZ31/ZrO_2 composites with a different volume fraction of the ZrO_2 addition after three cumulative FSP passes.

Interfacial Region Between ZrO_2 Particle and Mg Matrix

Figure 9a shows the TEM micrographs of homogeneously distributed ZrO_2 particles in the FSPed AZ31/ZrO_2 composite (Z3-3P specimen), and its selected area diffraction pattern is shown in **Figure 9b**. This also confirms the existence of ZrO2 particles in the Z3-3P specimen. The ZrO2 particles were uniformly dispersed in the Z3-3P specimen. **Figure 9c** shows the high magnification TEM micrographs, and the continuous and defect-free (micro-voids and cracks) interface was observed.

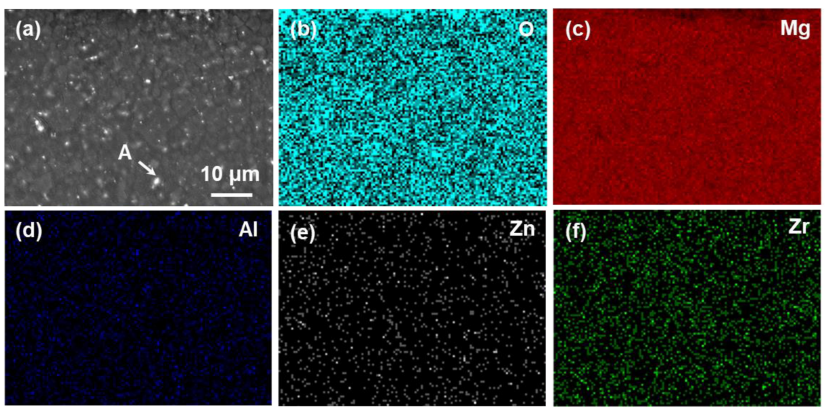

FIGURE 4 | EM-EDS mapping shows **(a)** the ZrO_2 particles embedded in matrix **(b–f)** color mapping of elements O, Mg, Al, Zn, and Zr of the SZ-center in FSPed AZ31/ZrO_2 composite (Z3-3P Specimen).

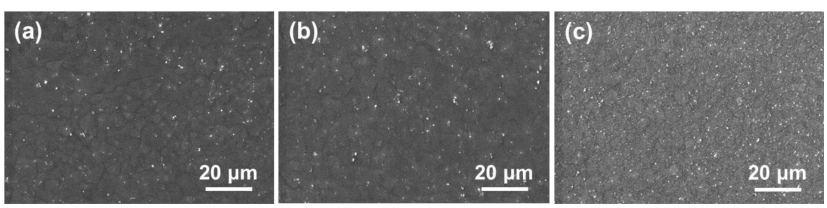

FIGURE 5 | SEM micrographs of SZ-center in FSPed AZ31/ZrO_2 composites: **(a)** Z1-3P specimen, **(b)** Z2-3P specimen, and **(c)** Z3-3P specimen.

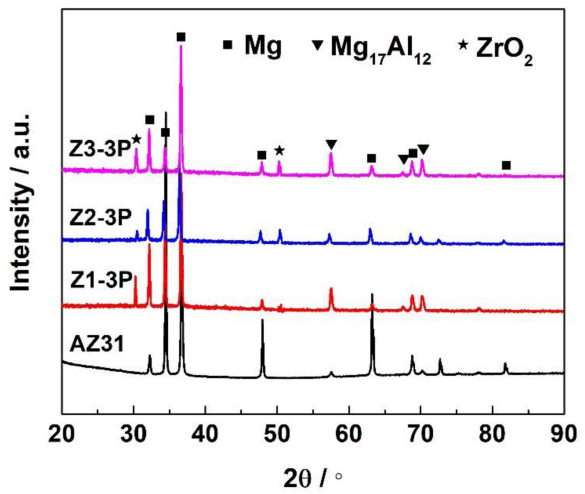

FIGURE 6 | XRD patterns of AZ31 alloy and FSPed AZ31/ZrO_2 composites.

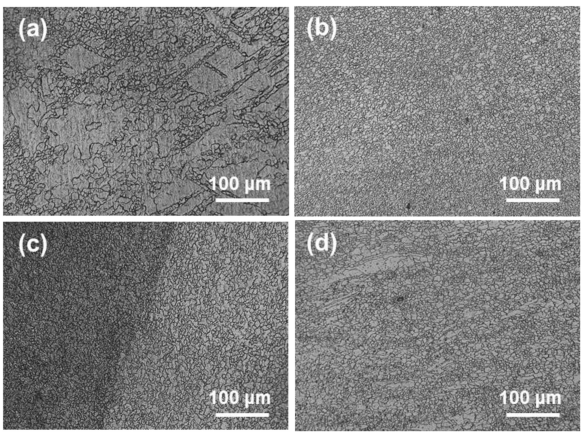

FIGURE 7 | OM of **(a)** AZ31 alloy, **(b)** SZ-center, **(c)** SZ/thermo-mechanically affected zone, and **(d)** TMAZ in FSPed AZ31/ZrO_2 composite (Z3-3P specimen).

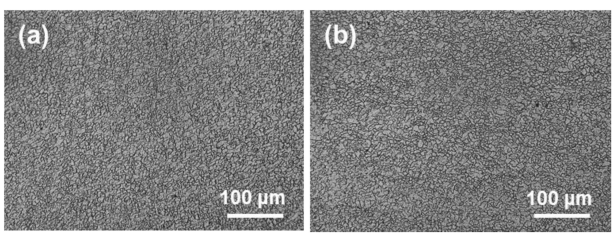

FIGURE 8 | OM of SZ-center in FSPed AZ31/ZrO_2 composites: **(a)** Z1-3P specimen and **(b)** Z2-3P specimen.

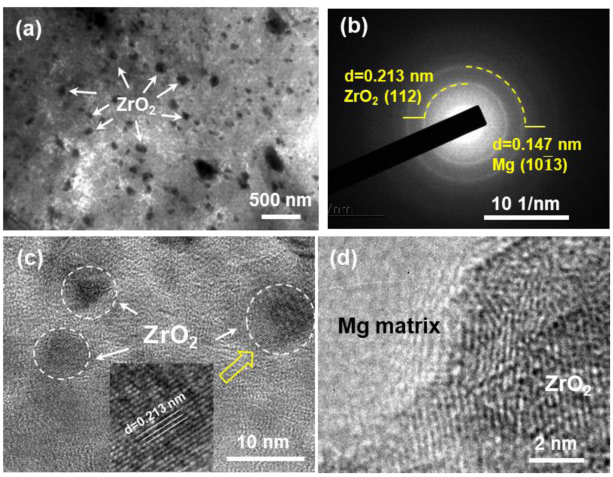

FIGURE 9 | TEM images of FSPed AZ31/ZrO_2 composite (Z3-3P specimen): **(a)** distribution of ZrO_2 particles, **(b)** selected area diffraction pattern, **(c)** high-resolution TEM micrograph, and **(d)** interface between the Mg matrix and ZrO_2 particle.

The distance of the layer-to-layer of the ZrO_2 particle is about 0.213 nm. **Figure 9d** shows the interfacial region between the ZrO_2 particle and the Mg matrix. The excellent interfacial bonding without any reaction product was observed. The well-bonding of AZ31-ZrO_2 is attributed to the lower heat generation and the severe plastic deformation during FSP.

Mechanical Properties of FSPed AZ31/ZrO_2 Composites

The microhardness mapping for the FSPed AZ31/ZrO_2 composites is shown in **Figures 10A–C**. The microhardness variations from SZ to base metal was pronounced, and the microhardness of SZ was the highest in FSPed AZ31/ZrO_2 composites compared with that in the base metal. The average microhardness values of SZ for Z1-3P specimen, Z2-3P specimen, and Z3-3P specimen were 74.02, 81.19, and 87.22 HV, respectively. The average microhardness of the AZ31 alloy was 60.14 HV. The microhardness of the FSPed AZ31/ZrO_2 composites improved compared with that of the AZ31 alloy. The average microhardness increased with the increase of ZrO_2 addition. At the same time, the region with higher hardness also increased with the increase of ZrO_2 addition, and the higher hardness within a larger area was observed in the Z3-3P specimen.

The engineering stress-strain curves of the AZ31 alloy and FSPed AZ31/ZrO_2 composites are shown in **Figure 10D**. The tensile properties of the AZ31 alloy and FSPed AZ31/ZrO_2 composites are shown in **Table 3**. The yield strength, tensile strength, and elongation of the FSPed AZ31/ZrO_2 composites (Z1-3P, Z2-3P, and Z3-3P specimens) increased to compare with that of the AZ31 alloy. The yield strength, tensile strength, and elongation of the FSPed AZ31/ZrO_2 composites increased with the increase of ZrO_2 addition. The FSP passes could affect the tensile properties of the FSPed AZ31/ZrO_2 composites, and the tensile properties of the FSPed Z3-1P, Z3-2P, and Z3-3P specimens increased with the increase of FSP passes. The yield strength, tensile strength, and elongation of the FSPed Z3-3P

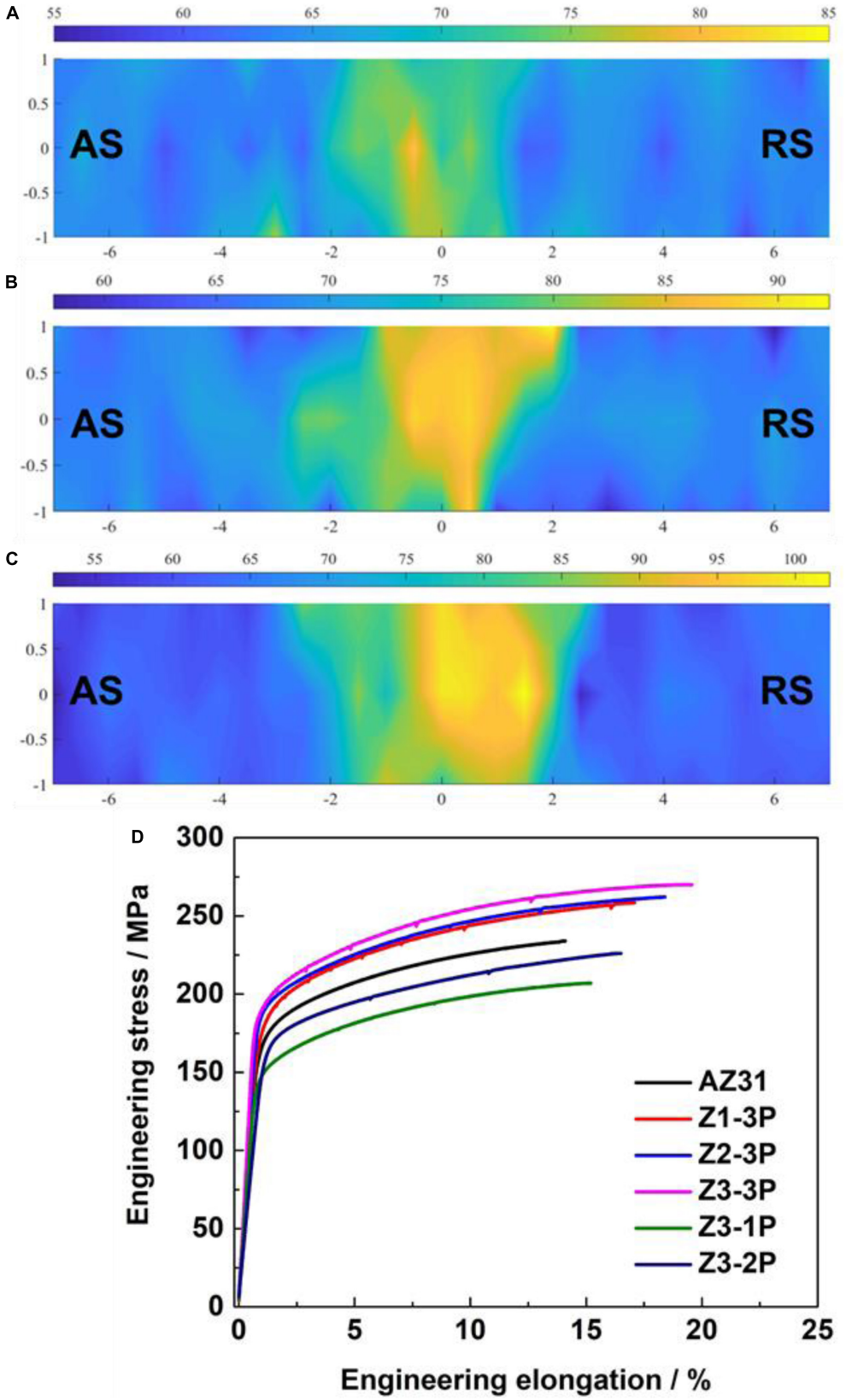

FIGURE 10 | Microhardness mapping of **(A)** Z1-3P specimen, **(B)** Z2-3P specimen, **(C)** Z3-3P specimen, and **(D)** engineering stress–strain curves of AZ31 alloy and FSPed AZ31/ZrO_2 composites.

TABLE 3 | Tensile properties of AZ31 alloy and AZ31/ZrO_2 composites.

Specimen	Y.S./MPa		T.S./MPa		EL/%	
AZ31	172 ± 4	100%	234 ± 6	100%	14.1 ± 0.5	100%
Z1-3P	187 ± 5	109%	258 ± 4	110%	17.1 ± 0.8	121%
Z2-3P	191 ± 4	111%	262 ± 5	112%	18.4 ± 0.5	130%
Z3-3P	201 ± 3	117%	270 ± 4	115%	19.6 ± 0.7	139%
Z3-1P	151 ± 7	88%	207 ± 6	88%	15.2 ± 1.1	108%
Z3-2P	167 ± 5	97%	226 ± 5	87%	16.5 ± 0.9	117%

specimen were 201 ± 3 and 270 ± 4 MPa and 19.6 ± 7%, respectively, which obtained the best tensile properties. The yield strength, tensile strength, and elongation improved by 17, 15, and 39%, respectively, compared with those of the AZ31 alloy.

The hardness of FSPed AZ31/ZrO_2 composites increased compared with that of the base metal. This is attributed to the effects of FSP on the microstructure refinements and the direct strengthening from ZrO_2 particles on the metal matrix (Hu et al., 2016; Rashad et al., 2016; Naseer et al., 2019). The grain refinement results in a higher resistance to the motion of dislocations, which could increase the hardness and strength. Based on the Hall–Petch relationship (Sharma S. et al., 2019), the finer grains could also improve the tensile properties of FSPed AZ31/ZrO_2 composites. At the same time, the ZrO_2 particles could act as obstacles against the dislocation movement (Zhang M. et al., 2020). Based on the microstructure of the Z1-3P, Z2-3P, and Z3-3P specimens, a similar grain size was observed in the SZ in these specimens. The larger area with higher microhardness was obtained in the SZ of the FSPed Z3-3P specimen. This indicated that the strengthening from reinforcement of ZrO_2 particles is predominant in the SZ of the FSPed specimens. The enhancement of strength can be explained by the Orowan strengthening mechanism (Xiang et al., 2017), which inhibits the dislocations from passing through the ZrO_2 particles. **Figure 11** shows that a large number of dislocations generated around ZrO_2 particles. It suggested that the ZrO_2 particles played the pinning effect on the dislocations. The strength could increase due to the accumulation of dislocations.

The good bonding between matrix and reinforcement is also important for the mechanical properties of composites (Sharma A. et al., 2019; Ajay Kumar et al., 2020). The improvement of the mechanical properties of Mg alloy composite reinforced by ZrO_2 particles is mainly determined by the interfacial bonding between the Mg matrix and ZrO_2 particles. In this study, the good bonding between the Mg matrix and the ZrO_2 particles was obtained in the FSPed AZ31/ZrO_2 composites, which is beneficial to the mechanical properties. The effective stress transfer between the matrix and reinforcement particles was obtained due to the strong interfacial bonding. At the same time, the distribution of ZrO_2 particles also affects the mechanical properties of the composites. The dispersed ZrO_2 particles with less aggregation were required for good mechanical properties (Xiang et al., 2017). The uniform dispersion of ZrO_2 particles was obtained in AZ31/ZrO_2 composites fabricated by high rotation speed FSP after three cumulative FSP passes. Thus, the tensile properties of the FSPed AZ31/ZrO_2 composites could increase

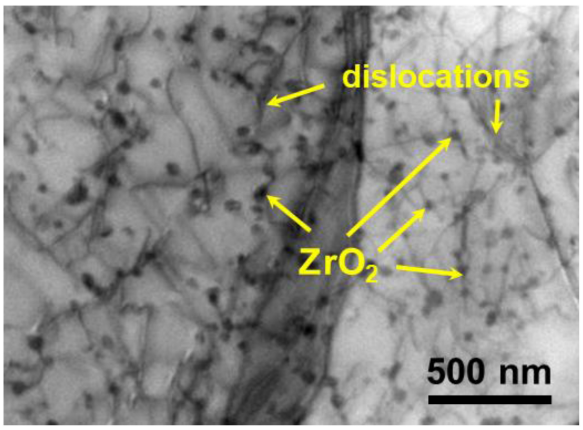

FIGURE 11 | Dislocations around ZrO_2 particles in FSPed AZ31/ZrO_2 composite (Z3-3P specimen).

with the increase of volume fraction of the ZrO_2 particles. More ZrO_2 particles were added, and these could improve the mechanical properties. The FSP passes played a key role in the particle distribution and mechanical properties. In general, the void formation at the particles occurred due to particle decohension in the soft matrix, which resulted in the fracture (Babout et al., 2004; Pineau et al., 2016). Firstly, the void nucleation can be discussed by energy, and the formation of the crack should exceed or equal the surface energy of new surface creating, which can be expressed as follows:

$$\sigma = \sqrt{2E\gamma_s/\pi c} \quad (1)$$

where E is the Young modulus, γ_s is surface interfacial energy, and c is half of the void length, and the particle size can replace the void length. This indicated that a large particle needs lower stress to create a new surface, and the coarse particles were weakly bonded to the matrix. The interfacial voids were easily formed at large agglomerations of ZrO_2 particles in the FSPed Z3-1P specimen, and the fine round particles need higher stress to form the interfacial voids. The agglomerations of ZrO_2 particles reduced in the FSPed Z3-2P specimen, and the strength and elongation increased while increasing the FSP passes to two passes. The best strength and elongation of the FSPed Z3-3P specimen were obtained due to the better distributions of ZrO_2 particles. It suggested that the FSPed Z3-3P specimen needs higher strain to form the voids compared with the FSPed Z3-1P and Z3-2P specimen.

CONCLUSION

In this work, the AZ31/2.14 vol% ZrO_2, AZ31/4.29 vol% ZrO_2, and AZ31/6.43 vol% ZrO_2 composites have been successfully fabricated by FSP with one pass, two multi-passes, and three multi-passes and high rotation speed. The microstructure, distribution of ZrO_2 particles, and mechanical properties of the FSPed AZ31/ZrO_2 composites were investigated. The effects of

FSP passes and ZrO_2 particles on the mechanical properties were discussed; the main conclusions generated are as follows:

(1) The fine microstructure was observed in the AZ31/ZrO_2 composites after three multi-pass FSPs. The average grain sizes of SZ-center in the AZ31/2.14 vol% ZrO_2, AZ31/4.29 vol% ZrO_2, and AZ31/6.43 vol% ZrO_2 composites were 8.46, 8.23, and 8.39 μm, respectively.
(2) The continuous clusters of ZrO_2 particles existed in the SZ of AZ31/6.43 vol% ZrO_2 composites after one FSP pass. The ZrO_2 particles did not distribute well in the matrix, and the agglomeration was unavoidable. The agglomeration of ZrO_2 particles reduced with the increase of FSP passes. The well-distributed ZrO_2 particles were obtained after three cumulative FSP passes.
(3) The hardness and tensile properties of the AZ31/ZrO_2 composites after three cumulative FSP passes were enhanced with the increase of volume fraction of the ZrO_2 particles. The tensile properties of the AZ31/ZrO_2 composites increased with the rise of FSP passes.
(4) The AZ31/6.43 vol% ZrO_2 composites after three cumulative FSP passes obtained the best tensile properties, which attributed to grain refinement from FSP, well-distributed ZrO_2 particles, and strong interfacial bonding between the Mg matrix and ZrO_2 particles.

DATA AVAILABILITY STATEMENT

The raw data supporting the conclusions of this article will be made available by the authors, without undue reservation, to any qualified researcher.

AUTHOR CONTRIBUTIONS

QZ and XL conceived and designed the experiments. JZ, LW, and SC performed the experiments. YJ and SL analyzed the data. QZ and HC wrote the manuscript. All authors contributed to the article and approved the submitted version.

FUNDING

This research was funded by the Priority Academic Program Development of Jiangsu Higher Education Institutions.

ACKNOWLEDGMENTS

We are grateful for financial support from the Priority Academic Program Development of Jiangsu Higher Education Institutions.

REFERENCES

Ajay Kumar, P., Madhu, H. C., Pariyar, A., Perugu, C. S., Kailas, S. V., Garg, U., et al. (2020). Friction stir processing of squeeze cast A356 with surface compacted graphene nanoplatelets (GNPs) for the synthesis of metal matrix composites. *Mater. Sci. Eng. A* 769:138517. doi: 10.1016/j.msea.2019.138517

Arab, M., and Marashi, S. P. H. (2019). Effect of graphene nanoplatelets (GNPs) content on improvement of mechanical and tribological properties of AZ31 Mg matrix nanocomposite. *Tribol. Intl.* 132, 1–10. doi: 10.1016/j.triboint.2018.11.023

Babout, L., Brechet, Y., Maire, E., and Fougères, R. (2004). On the competition between particle fracture and particle decohesion in metal matrix composites. *Acta Mater.* 52, 4517–4525. doi: 10.1016/j.actamat.2004.06.009

Balakrishnan, M., Dinaharan, I., Palanivel, R., and Sivaprakasam, R. (2015). Synthesize of AZ31/TiC magnesium matrix composites using friction stir processing. *J. Magnes. Alloys* 3, 76–78. doi: 10.1016/j.jma.2014.12.007

Barati, M., Abbasi, M., and Abedini, M. (2019). The effects of friction stir processing and friction stir vibration processing on mechanical, wear and corrosion characteristics of Al6061/SiO2 surface composite. *J. Manuf. Process.* 45, 491–497. doi: 10.1016/j.jmapro.2019.07.034

Chen, L., Li, J., Zhang, Y., Zhang, L. C., Lu, W., Zhang, L., et al. (2015). Effects of alloyed Si on the autoclave corrosion performance and periodic corrosion kinetics in Zr-Sn-Nb-Fe-O alloys. *Corros. Sci.* 100, 651–662. doi: 10.1016/j.corsci.2015.08.043

Chen, S., Zhou, Y., Xue, J., Ni, R., Guo, Y., and Dong, J. (2017). High rotation speed friction stir welding for 2014 aluminum alloy thin sheets. *J. of Materi Eng and Perform* 26, 1337–1345. doi: 10.1007/s11665-017-2524-y

Del Valle, J. A., Rey, P., Gesto, D., Verdera, D., Jiménez, J. A., and Ruano, O. A. (2015). Mechanical properties of ultra-fine grained AZ91 magnesium alloy processed by friction stir processing. *Mater. Sci. Eng. A* 628, 198–206. doi: 10.1016/j.msea.2015.01.030

Hanas, T., Sampath Kumar, T. S., Perumal, G., Doble, M., and Ramakrishna, S. (2018). Electrospun PCL/HA coated friction stir processed AZ31/HA composites for degradable implant applications. *J. Mater. Process. Technol.* 252, 398–406. doi: 10.1016/j.jmatprotec.2017.10.009

Hashemi, R., and Hussain, G. (2015). Wear performance of Al/TiN dispersion strengthened surface composite produced through friction stir process: a comparison of tool geometries and number of passes. *Wear* 324–325, 45–54. doi: 10.1016/j.wear.2014.11.024

Hu, Z., Tong, G., Lin, D., Chen, C., Guo, H., Xu, J., et al. (2016). Graphene-reinforced metal matrix nanocomposites–a review. *Mater. Sci. Technol.* 32, 930–953. doi: 10.1080/02670836.2015.1104018

Khodabakhshi, F., Arab, S. M., Švec, P., and Gerlich, A. P. (2017). Wear performance of Al/TiN dispersion strengthened surface composite produced through friction stir process: a comparison of tool geometries and number of passes. *Mater. Charact.* 132, 92–107. doi: 10.1016/j.wear.2014.11.024

Li, L. L., Chen, T. J., Zhang, S. Q., and Yan, F. Y. (2017). Electrochemical cold drawing of in situ Mg2Sip/AM60B composite: a comparison with the AM60B alloy. *J. Mater. Process. Technol.* 240, 33–41. doi: 10.1016/j.jmatprotec.2016.09.007

Liang, J., Li, H., Qi, L., Tian, W., Li, X., Chao, X., et al. (2017). Fabrication and mechanical properties of CNTs/Mg composites prepared by combining friction stir processing and ultrasonic assisted extrusion. *J. Alloys Compd.* 728, 282–288. doi: 10.1016/j.jallcom.2017.09.009

Liu, F., Ji, Y., Sun, Z., Liu, J., Bai, Y., and Shen, Z. (2020). Enhancing corrosion resistance and mechanical properties of AZ31 magnesium alloy by friction stir processing with the same speed ratio. *J. Alloys Compd.* 829:154452. doi: 10.1016/j.jallcom.2020.154452

Mazaheri, Y., Jalilvand, M. M., Heidarpour, A., and Jahani, A. R. (2020). Tribological behavior of AZ31/ZrO2 surface nanocomposites developed by friction stir processing. *Tribol. Int.* 143:106062. doi: 10.1016/j.triboint.2019.106062

Meng, L., Hu, X., Wang, X., Zhang, C., Shi, H., Xiang, Y., et al. (2018). Graphene nanoplatelets reinforced Mg matrix composite with enhanced mechanical properties by structure construction. *Mater. Sci. Eng. A* 733, 414–418. doi: 10.1016/j.msea.2018.07.056

Naseer, A., Ahmad, F., Aslam, M., Guan, B. H., Harun, W. S. W., Muhamad, N., et al. (2019). A review of processing techniques for graphene-reinforced metal matrix composites. *Mater. Manuf. Process.* 34, 957–985. doi: 10.1080/10426914.2019.1615080

Navazani, M., and Dehghani, K. (2016). Fabrication of Mg-ZrO2 surface layer composites by friction stir processing. *J. Mater. Process. Technol.* 229, 439–449. doi: 10.1016/j.jmatprotec.2015.09.047

Pineau, A., Benzerga, A., and Pardoen, A. (2016). T. failure of metals i: brittle and ductile fracture. . *Acta Mater.* 107, 424–483. doi: 10.1016/j.actamat.2015.12.034

Rashad, M., Pan, F., and Asif, M. (2016). Exploring mechanical behavior of Mg–6Zn alloy reinforced with graphene nanoplatelets. *Mater. Sci. Eng. A* 649, 263–269. doi: 10.1016/j.msea.2015.10.009

Shahin, M., Munir, K., Wen, C., and Li, Y. (2020). Magnesium-based composites reinforced with graphene nanoplatelets as biodegradable implant materials. *J. Alloys Compd.* 828:154461. doi: 10.1016/j.jallcom.2020.154461

Shang, J., Ke, L., Liu, F., Lv, F., and Xing, L. (2019). Aging behavior of nano SiC particles reinforced AZ91D composite fabricated via friction stir processing. *J. Alloys Compd.* 797, 1240–1248. doi: 10.1016/j.jallcom.2019.04.280

Sharma, A., Sharma, V. M., Sahoo, B., Pal, S. K., and Paul, J. (2019). Effect of multiple micro channel reinforcement filling strategy on Al6061-graphene nanocomposite fabricated through friction stir processing. *J. Manuf. Process.* 37, 53–70. doi: 10.1016/j.jmapro.2018.11.009

Sharma, S., Handa, A., Singh, S. S., and Verma, D. (2019). Influence of tool rotation speeds on mechanical and morphological properties of friction stir processed nano hybrid composite of MWCNT-Graphene-AZ31 magnesium. *J. Magnes. Alloys* 7, 487–500. doi: 10.1016/j.jma.2019.07.001

Suh, J., Victoria-Hernández, J., Letzig, D., Golle, R., and Volk, W. (2016). Effect of processing route on texture and cold formability of AZ31 Mg alloy sheets processed by ECAP. *Mater. Sci. Eng. A* 669, 159–170. doi: 10.1016/j.msea.2016.05.027

Vahedi, F., Zarei-Hanzaki, A., Salandari-Rabori, A., Abedi, H. R., Razaghian, A., and Minarik, P. (2020). Microstructural evolution and mechanical properties of thermomechanically processed AZ31 magnesium alloy reinforced by micro-graphite and nano-graphene particles. *J. Alloys Compd.* 815:152231. doi: 10.1016/j.jallcom.2019.152231

Xiang, S. L., Gupta, M., Wang, X. J., Wang, L. D., Hu, X. S., and Wu, K. (2017). Enhanced overall strength and ductility of magnesium matrix composites by low content of graphene nanoplatelets. *Compos. Part A Appl. Sci. Manuf.* 100, 183–193. doi: 10.1016/j.compositesa.2017.05.011

Yu, W., Zhao, H., and Hu, X. (2018). Anisotropic mechanical and physical properties in textured Ti2AlC reinforced AZ91D magnesium composite. *J. Alloys Compd.* 732, 894–901. doi: 10.1016/j.jallcom.2017.10.255

Zang, Q. H., Chen, H. M., Lan, F. Y., Zhang, J., and Jin, Y. X. (2017). Effect of friction stir processing on microstructure and damping capacity of AZ31 alloy. *J. Cent. South Univ.* 24, 1034–1039. doi: 10.1007/s11771-017-3506-3509

Zhang, J., Xi, G., Wan, X., and Fang, C. (2017). The dislocation-twin interaction and evolution of twin boundary in AZ31 Mg alloy. *Acta Mater.* 133, 208–216. doi: 10.1016/j.actamat.2017.05.034

Zhang, L., Luo, X., Liu, J., Leng, Y., and An, L. (2018). Dry sliding wear behavior of Mg-SiC nanocomposites with high volume fractions of reinforcement. *Mater. Lett.* 228, 112–115. doi: 10.1016/j.matlet.2018.05.114

Zhang, L. C., and Chen, L. Y. (2019). A review on biomedical titanium alloys: recent progress and prospect. *Adv. Eng. Mater.* 21:1801215. doi: 10.1002/adem.201801215

Zhang, L. C., Chen, L. Y., and Wang, L. (2020). Surface modification of titanium and titanium alloys: technologies, developments and future interests. *Adv. Eng. Mater.* 22:1901258. doi: 10.1002/adem.201901258

Zhang, M., Shen, M., and Jia, J. (2020). Processing and mechanical properties of Mg-2.8*Al*-0.8Zn alloy containing bimodal size distribution. *J. Mater. Res. Technol.* 9, 2495–2505. doi: 10.1016/j.jmrt.2019.12.080

Zhang, M., Li, Y. N., Zhang, F. C., Wang, X. B., Chen, L. Y., and Yang, Z. N. (2017). Effect of annealing treatment on the microstructure and mechanical properties of a duplex Zr-2.5*Nb alloy*. *Mater. Sci. Eng. A* 706, 236–241. doi: 10.1016/j.msea.2017.08.107

Conflict of Interest: XL was employed by the company Shandong Heavy Machinery Co., Ltd.

The remaining authors declare that the research was conducted in the absence of any commercial or financial relationships that could be construed as a potential conflict of interest.